

Electronic Supplementary Information

Electronic Redistribution through the Interface of MnCo₂O₄-Ni₃N Nano-Urchins prompted rapid In- Situ Phase Transformation for Enhanced Oxygen Evolution Reaction

*Ashish Gaur[†], Aashi[†], Joel Mathew John, Vikas Pundir, Rajdeep Kaur, Jatin Sharma,
Kaustubhi Gupta, Chandan Bera and Vivek Bagchi**

[†] = both the authors contributed equally

*Institute of Nano Science and Technology, Sector-81, Knowledge City, Sahibzada Ajit Singh
Nagar, Punjab, Pin - 140306, India*

S1.1. Physical characterization

S1.2 Electrochemical Analysis

S2.1. Wide scan XPS spectra of $\text{MnCo}_2\text{O}_4\text{-Ni}_3\text{N}$, MnCo_2O_4 and Ni_3N

S2.2. O1s XPS spectra of $\text{MnCo}_2\text{O}_4\text{-NiOOH}$

S3.1. Drop shape analysis of bare nickel foam

S3.2. Drop shape analysis of the MnCo_2O_4 and NiOOH

S4.1. Cyclic Voltammetry curve for the calculation of C_{dl}

S4.2. ECSA normalized LSV curve of all the catalysts.

S4.3. Comparison of the recently reported non-noble metal based catalyst

S4.4. After stability XPS spectra of $\text{MnCo}_2\text{O}_4\text{-NiOOH}$

S5. Details discussion about DFT calculations

S6. Table containing comparison of cell potential of recently reported catalysts.

S1.1. Physical characterization

The Bruker Eco D8 ADVANCE X Powder X-ray diffractometer was used to investigate the structural properties of $\text{MnCo}_2\text{O}_4\text{-Ni}_3\text{N}$. The diffractometer consists of a Ni filter that provides Cu K radiation ($\lambda = 1.54056$, 40 kV, and 25 mA) in the 2θ range of $10^\circ\text{-}80^\circ$ with a rise of 0.00190/step. The morphological examination of the heterostructures is performed using a JEOL JSM-7600F (FESEM) scanning electron microscope SEM equipped with an energy-dispersive X-ray diffractometer (Bruker). Transmission electron microscopy (TEM) JEOL-2100 operating at 200 kV was used to analyse the length and breadth of the $\text{MnCo}_2\text{O}_4\text{-Ni}_3\text{N}$, MnCo_2O_4 and Ni_3N and $\text{MnCo}_2\text{O}_4\text{-NiOOH}$ heterostructure. X-Ray photoelectron (XPS) spectroscopy was executed on a K-Alpha plus XPS system of Thermo Fisher Scientific instruments in an ultrahigh vacuum chamber (7×10^{-9} torr) using Al-K α radiation (1486.6 eV).

S1.2. Electrochemical Analysis

At a temperature of 25°C, all electrochemical measurements were performed on Metrohm auto lab electrochemical workstation. A graphite electrode serves as a counter electrode, and a saturated Ag/AgCl electrode serves as a reference electrode in the traditional three-electrode arrangement. All of the polarisation data was obtained in 1 M KOH at a scan rate of 5 mV s⁻¹. $E_{\text{RHE}} = E_{\text{Ag/AgCl}} + 0.197 + 0.059 \times \text{pH}$ is the equation used to convert to a reversible hydrogen electrode. The Tafel slope was determined by plotting the polarisation curve again and fitting the linear portion of the Tafel plot to the Tafel equation ($\eta = b \log(j) + a$). The elimination of Ohmic drop was used to correct the iR_s , as stated by the equation $\eta_{\text{corrected}} = \eta - iR_s$, where R_s signifies the solution resistance. Electrochemical impedance spectroscopy (EIS) was carried out at a frequency range of 1 to 100000 Hz with an overpotential of 200 mV. We employed chronoamperometry for the stability study. The double layer capacitance was determined using CV scans in a non-Faradaic potential range of as-prepared catalyst electrodes in 1 M KOH at a scan rate of 20 to 200 mV/s for the calculation of electrochemically active surface area (ECSA). Half of the variations in current density ($J = (J_{\text{anodic}} - J_{\text{cathodic}})$) shown against scan rate at a potential of 1.16 V versus RHE fit to a linear regression that allows the measurement of double layer capacitance (Cdl). The faradic efficiency was calculated by dividing the experimental oxygen evolution by the theoretical oxygen evolution.

Calculation of ECSA:

The ECSAs of the samples have been determined based on the measured C_{dl} . The current observed in the non-Faradaic zone is a result of the charging of the double layer and exhibits a linear correlation with the active surface area. In general, the specific capacitance of a flat surface area measuring 1cm^2 is typically equal to a C_s value ranging from 20 to 60 $\mu\text{F cm}^{-2}$, with an average value of 40 $\mu\text{F cm}^{-2}$. Therefore, the Cdl can be transformed into the ECSA as follows.

$$\text{ECSA} = C_{dl}/2C_s$$

S2.1. Wide scan XPS spectra of $\text{MnCo}_2\text{O}_4\text{-Ni}_3\text{N}$, MnCo_2O_4 and Ni_3N :

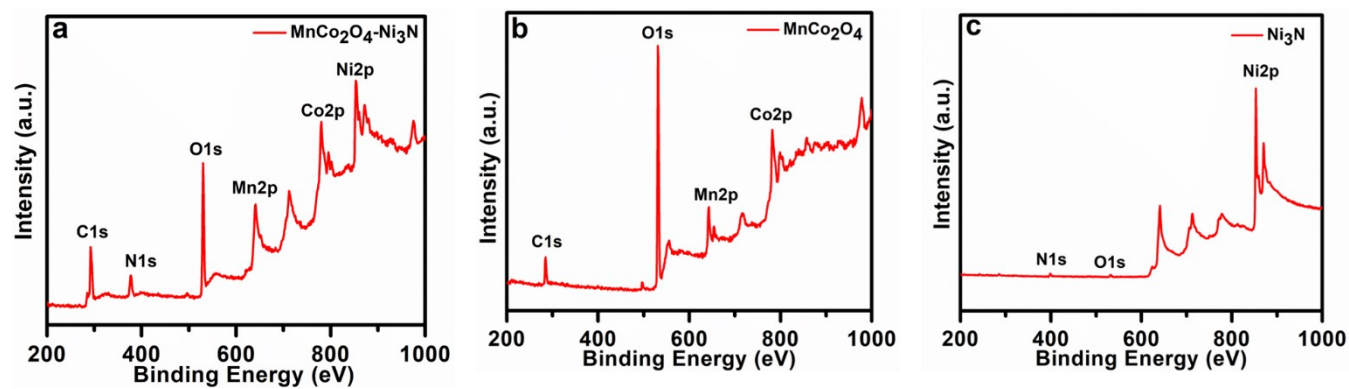


Figure S1. Wide scan XPS spectra of $\text{MnCo}_2\text{O}_4\text{-Ni}_3\text{N}$, MnCo_2O_4 and Ni_3N

S2.2. O1s XPS spectra of MnCo₂O₄-NiOOH

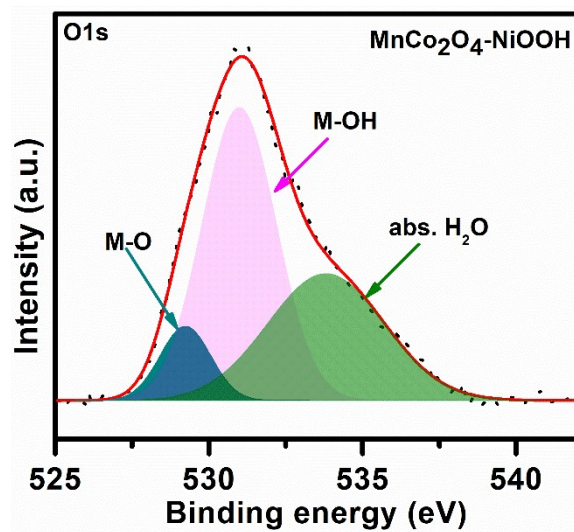


Figure S2. High resolution XPS spectra of O1s in MnCo₂O₄-NiOOH

S3.1. Drop shape analysis of bare nickel foam

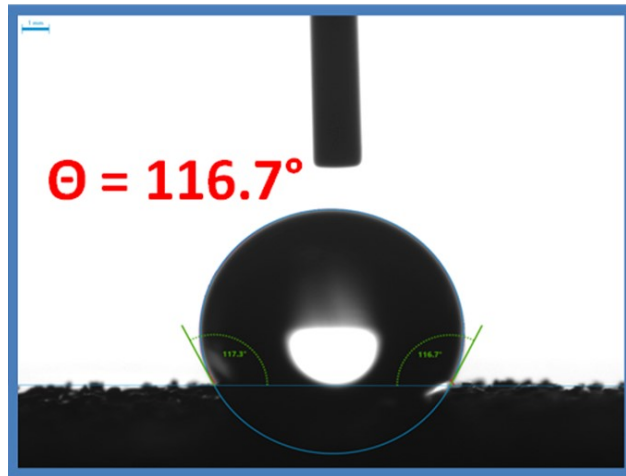


Figure S3. Drop shape analysis of bare NF

ESI S3.2. Drop shape analysis of MnCo_2O_4 and NiOOH .

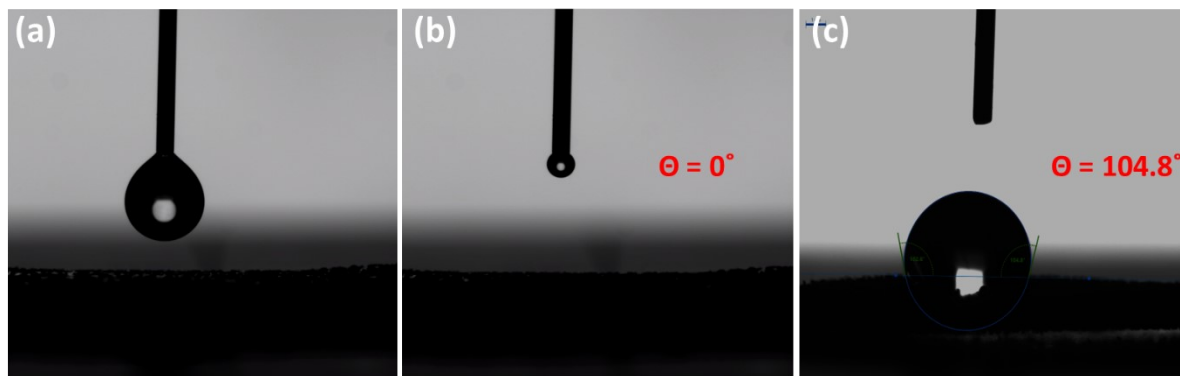


Figure S4. Drop shape analysis of NiOOH and MnCo_2O_4

S4.1. Cyclic Voltammetry curve for the calculation of C_{dl}

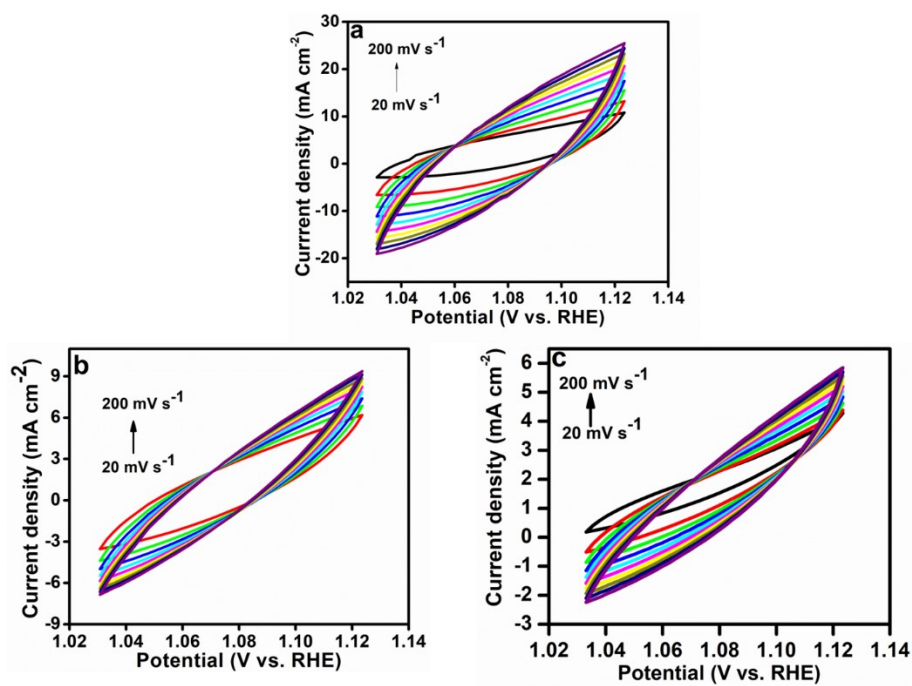


Figure S5. Cyclic voltammetry curve of (a) MnCo₂O₄-NiOOH, (b) NiOOH and (c) MnCo₂O₄ for the calculation of C_{dl}

S4.2. ECSA normalized LSV curve of all the catalysts.

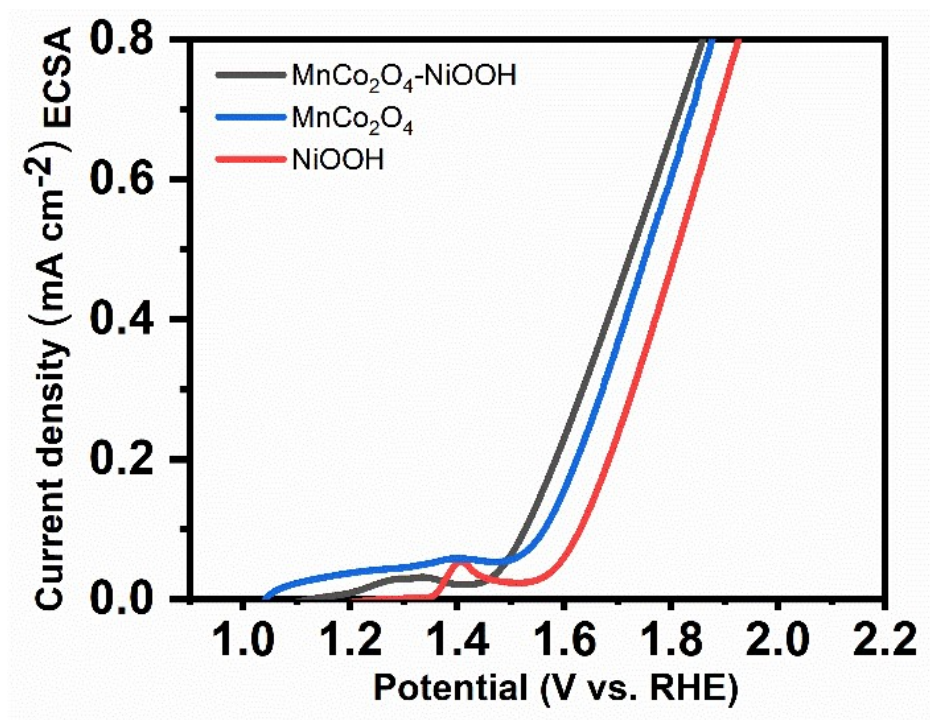


Figure S6. ECSA normalized LSV curve of all the catalysts.

S4.3. Comparison of the recently reported non-noble metal-based catalyst

Catalyst Name	Overpotential (mV)@10 mA cm⁻²	References
(Co-O)-MoS_{0.9}	283	1
Co₁Mo₁Ni_{0.5} Pi	272	2
Co_{0.50}Fe_{0.50}-LDH	270	3
Co-THB/CP	263	4
Cr-Cu/CoO_x	252	5
SCI-350	250	6
Cd-MOF 1	233	7

Table S1. Comparison of the recently reported non-noble metal-based catalyst.

S4.4. XPS analysis of $\text{MnCo}_2\text{O}_4\text{-NiOOH}$ after stability test:

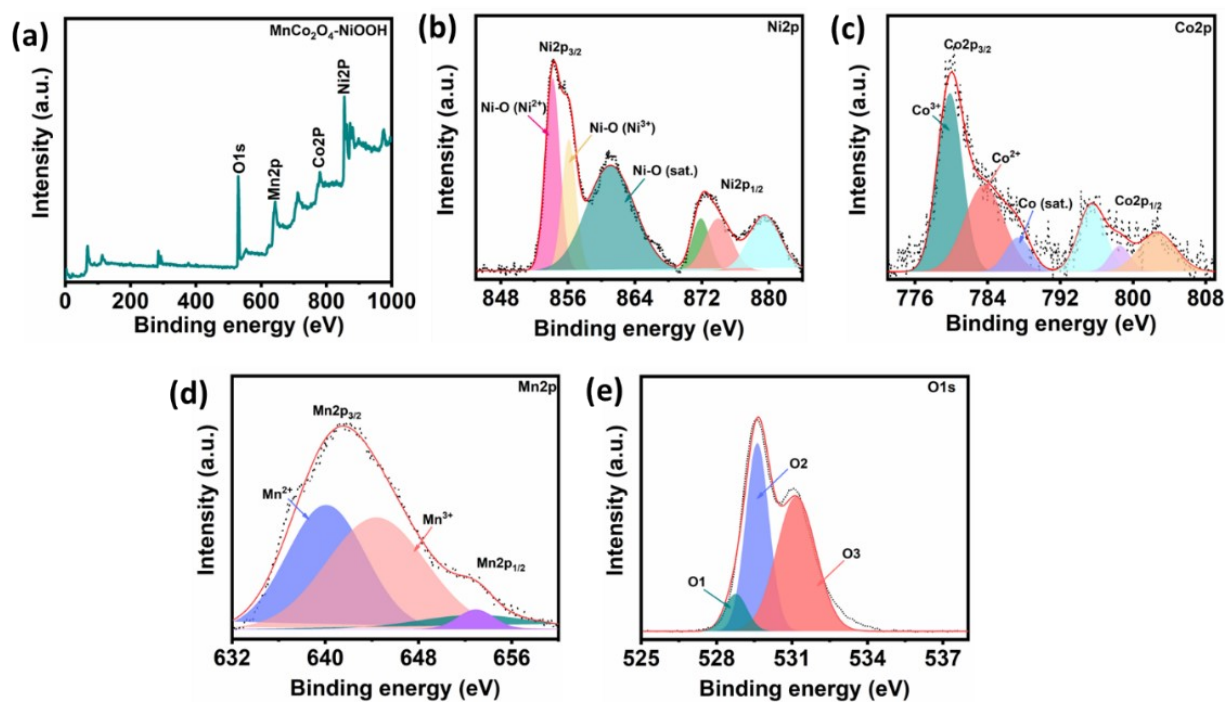
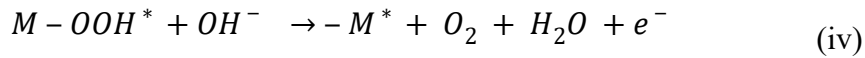
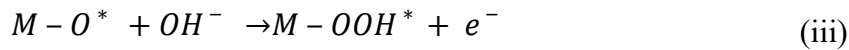
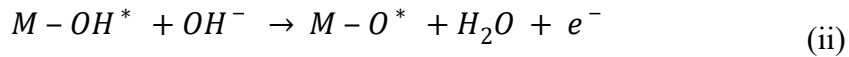
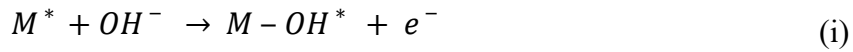


Figure S7. XPS analysis of $\text{MnCo}_2\text{O}_4\text{-NiOOH}$ after stability test. (a) wide scan, high resolution XPS spectra of (b) Ni2p, (c) Co2p, (d) Mn2p, (e) O1s.

S5. Details discussion about DFT calculations:

The Vienna Ab initio Simulation Package (VASP) was used to do density functional theory (DFT) simulations to look into the catalyst's active site and Gibbs free energy. [8] A 15 Å vacuum was supplied in the Z- direction to prevent periodic imaging contact, and a supercell made up of 77 atoms with the properties of a=8.5, b=8.5, and c=25 was formed. The cutoff energy was selected at 520 eV and a 7 7 1-center K-mesh was used. It took structural optimization till the forces and energy convergence were within 0.01 eV⁻¹ and the energy convergence reached 10⁻⁴ eV.

The OER mechanism consists of four stages in an alkaline media, which are explained below:



where, M is the metal's active site and OH*, O*, and OOH* are the intermediates adsorbed on the active sites.

The following equations were used to compute the adsorption energies of each step in order to identify the active site:

$$\Delta E_{OH^*} = E_{OH^*} - E^* - E_{H_2O} + \frac{1}{2}E_{H_2}$$

$$\Delta E_{O^*} = E_{O^*} - E^* - E_{H_2O} + E_{H_2}$$

$$\Delta E_{OOH^*} = E_{OOH^*} - E^* - 2E_{H_2O} + \frac{3}{2}E_{H_2}$$

The formula below was used to calculate the adsorption Gibbs free energy (G) for OER, which is a crucial sign of the process's spontaneity [9-10]

$$\Delta G_{ads} = \Delta E_{ads} + \Delta E_{ZPE} - T\Delta S + \Delta G_u + \Delta G_{pH}$$

The terms EZPE, S, and T in the equation above stand for the system's difference in zero-point energy, entropy, and temperature, respectively. For the sake of simplification, EZPE and TS were taken to be zero. G_u stands for the applied electrode potential, where $G_u = eU$, where e signifying the quantity of electron transfers and U for the electrode potential. G_{pH} is equal to $-k_B T \ln[H^+] = 2.303k_B T * pH$, where B is the Boltzmann constant and T is the system temperature. The Gibb's energy of each intermediate was estimated under standard conditions (pH=0, T=298.15K) using the following equation:

$$\Delta G_1 = \Delta E_{OH^*}$$

$$\Delta G_2 = \Delta E_{O^*} - \Delta E_{OH^*}$$

$$\Delta G_3 = \Delta E_{OOH^*} - \Delta E_{O^*}$$

$$\Delta G_4 = 4.92 - (\Delta G_1 + \Delta G_2 + \Delta G_3)$$

Table S2: Total energy and adsorption energy of different adsorbates on the surface of the $MnCo_2O_4$ electrode.

Surface	Total Energy (eV)	Adsorption energy (eV)
$MnCo_2O_4$	-236.69	-
Mn-OH*	-246.36	1.81
Mn-O*	-242.9	1.88

Mn-OOH*	250.6	5.66
Co-OH*	-249.7	-1.53
Co-O*	-244.5	0.277
Co-OOH*	-254.2	2.06

Table S3. Total energy and adsorption energy of different adsorbates on the surface of the NiOOH electrode.

Surface	Total Energy (eV)	Adsorption energy (eV)
NiOOH	-219.3	-
Ni-OH*	-230.31	0.47
Ni-O*	-224.45	2.94
Ni-OOH*	-234.64	4.23

Table S4. Total energy and adsorption energy of different adsorbates on the surface of the MnCo₂O₄-NiOOH electrode.

Surface	Total Energy (eV)	Adsorption energy (eV)
MnCo ₂ O ₄ -NiOOH	-456.248	-
Ni-OH*	-459.235	2.268
Ni-O*	-464.901	4.158
Ni-OOH*	-469.407	5.24
H ₂ O	-14.8747541	-
H ₂	-6.787373128	-

Table S5. Gibb's free energy values of MnCo₂O₄, NiOOH, and MnCo₂O₄-Ni*OOH at different adsorption sites.

Surface		ΔG_1 (eV)	ΔG_2 (eV)	ΔG_3 (eV)	ΔG_4 (eV)
Mn*Co ₂ O ₄	At U=0	1.81	0.06	3.78	-0.73
	At U= 1.23	0.58	-1.16	2.55	-1.97
MnCo* ₂ O ₄	At U=0	-1.53	1.8	1.78	2.86
	At U= 1.23	-2.76	0.58	0.55	1.63
Ni*OOH	At U=0	0.47	2.46	1.29	0.69
	At U= 1.23	-0.76	1.23	0.06	-0.53
MnCo ₂ O ₄ -Ni*OOH	At U=0	2.26	1.89	1.09	-0.32
	At U= 1.23	1.03	0.66	0.14	-1.55

Table S6. Table containing comparison of cell potential of recently reported catalysts.

Cell	Cell Potential	Reference
Co-ZnRuOx Co-ZnRuOx	1.48	11
Ni ₃ Fe-NC Ni ₃ Fe-NC	1.49	12
S- Fe- Ni S- Fe- Ni	1.49	13
MOF- Mo _{SA} -W _{SA} MOF- Mo _{SA} -W _{SA}	1.50	14
MoSe ₂ @NiCo ₂ Se ₄ MoSe ₂ @NiCo ₂ Se ₄	1.51	15
Cr-Cu/CoOx Cr-Cu/CoOx	1.51	16
AuFe ₁ NC/NF AuFe ₁ NC/NF	1.52	17
W ₂ N ₃ /Fe ₂ N W ₂ N ₃ /Fe ₂ N	1.52	18
Co(OH) ₂ -La(OH) ₃ @Cu Co(OH) ₂ -La(OH) ₃ @Cu	1.56	19
V ₂ C-Mxene V ₂ C-Mxene	1.57	20
CPF-Fe/Ni CPF-Fe/Ni	1.57	21
Ni-250-2@NF Ni-250-2@NF	1.58	22
CoMoNiPi CoMoNiPi	1.59	23
N-NiMoO ₄ /Ni/CNTs N-NiMoO ₄ /Ni/CNTs	1.64	24
NiCo-LDH@NH ₂ -UIO-66 NiCo-LDH@NH ₂ -UIO-66	1.65	25

References

1. Pan, M., Zhang, X., Pan, C., Wang, J. and Pan, B., 2023. Identification of Co–O–Mo Active Centers on Co-Doped MoS₂ Electrocatalyst. *ACS Applied Materials & Interfaces*, 15(15), pp.19695-19704.
2. Viswanathan, P. and Kim, K., 2023. In Situ Surface Restructuring of Amorphous Ni-Doped CoMo Phosphate-Based Three-Dimensional Networked Nanosheets: Highly Efficient and Durable Electrocatalyst for Overall Alkaline Water Splitting. *ACS Applied Materials & Interfaces*, 15(13), pp.16571-16583.
3. Shankar Naik, S., Theerthagiri, J., Nogueira, F.S., Lee, S.J., Min, A., Kim, G.A., Maia, G., Pinto, L.M. and Choi, M.Y., 2023. Dual-cation-coordinated CoFe-layered double-hydroxide nanosheets using the pulsed laser ablation technique for efficient electrochemical water splitting: mechanistic screening by in situ/operando raman and density functional theory calculations. *ACS Catalysis*, 13(2), pp.1477-1491.
4. Lu, C., Zhu, D., Su, Y., Xu, H. and Gu, C., 2023. Linear Conjugated Coordination Polymers for Electrocatalytic Oxygen Evolution Reaction. *Small*, p.2207720.
5. Mu, X., Wang, K., Lv, K., Feng, B., Yu, X., Li, L., Zhang, X., Yang, X. and Lu, Z., 2023. Doping of Cr to Regulate the Valence State of Cu and Co Contributes to Efficient Water Splitting. *ACS Applied Materials & Interfaces*, 15(13), pp.16552-16561.
6. Guo, H., Yang, Y., Yang, G., Cao, X., Yan, N., Li, Z., Chen, E., Tang, L., Peng, M., Shi, L. and Xie, S., 2023. Ex Situ Reconstruction-Shaped Ir/CoO/Perovskite Heterojunction for Boosted Water Oxidation Reaction. *ACS catalysis*, 13(7), pp.5007-5019.
7. Wu, R., Wang, J., Wang, L., Xu, C., Luo, R., Shao, F., Zhang, X. and Fan, Y., 2023. Three-Dimensional Cadmium–Organic Framework with Dual Functions of Oxygen Evolution in Water Splitting and Fenton-like Photocatalytic Removal of Organic Pollutants. *Inorganic Chemistry*, 62(16), pp.6339-6351.
8. Kresse, G.; Furthmüller, J., Efficiency of ab-initio total energy calculations for metals and semiconductors using a plane-wave basis set. *Computational materials science*, 6 (1), 15-50.
9. Ahmed, Z.; Krishankant; Rai, R.; Kumar, R.; Maruyama, T.; Bera, C.; Bagchi, V., Unraveling a Graphene Exfoliation Technique Analogy in the Making of Ultrathin Nickel–Iron Oxyhydroxides@ Nickel Foam to Promote the OER. *ACS Applied Materials & Interfaces*, 13 (46), 55281-55291
10. Aashi; Alagar, S.; Krishankant; Gaur, A.; Bera, C.; Bagchi, V., Rapid synthesis of a CuZn-MOF via controlled electrodeposition: manifesting enhanced overall electrocatalytic water splitting. *Sustainable Energy & Fuels*
11. Liu, D., Wu, Z., Liu, J., Gu, H., Li, Y., Li, X., Liu, S., Liu, S. and Zhang, J., 2023. Heteroatom Doped Amorphous/Crystalline Ruthenium Oxide Nanocages as a Remarkable Bifunctional Electrocatalyst for Overall Water Splitting. *Small*, 19(11), p.2207235.
12. Guo, M., Meng, H., Jin, J. and Mi, J., 2023. Amine-assisted synthesis of the Ni₃Fe alloy encapsulated in nitrogen-doped carbon for high-performance water splitting. *Journal of Materials Chemistry A*, 11(12), pp.6452-6464.
13. Zang, Z., Guo, Q., Li, X., Cheng, Y., Li, L., Yu, X., Lu, Z., Yang, X., Zhang, X. and Liu, H., 2023. Construction of a S and Fe co-regulated metal Ni electrocatalyst for efficient alkaline overall water splitting. *Journal of Materials Chemistry A*, 11(9), pp.4661-4671.
14. Cheng, C.C., Lin, T.Y., Ting, Y.C., Lin, S.H., Choi, Y. and Lu, S.Y., 2023. Metal-organic frameworks stabilized Mo and W binary single-atom catalysts as high performance bifunctional electrocatalysts for water electrolysis. *Nano Energy*, 112, p.108450.
15. Majumdar, A., Dutta, P., Sikdar, A., Lee, H., Ghosh, D., Jha, S.N., Tripathi, S., Oh, Y. and Maiti, U.N., 2022. Impact of atomic rearrangement and single atom stabilization on MoSe₂@

- NiCo₂Se₄ heterostructure catalyst for efficient overall water splitting. *Small*, *18*(19), p.2200622.
16. Mu, X., Wang, K., Lv, K., Feng, B., Yu, X., Li, L., Zhang, X., Yang, X. and Lu, Z., 2023. Doping of Cr to Regulate the Valence State of Cu and Co Contributes to Efficient Water Splitting. *ACS Applied Materials & Interfaces*, *15*(13), pp.16552-16561.
 17. Sun, Y., Luo, J., Zhang, M., Li, J., Yu, J., Lu, S., Song, W., Wei, Y., Li, Z. and Liu, J., 2023. Electron Delocalization of Au Nanoclusters Triggered by Fe Single Atoms Boosts Alkaline Overall Water Splitting. *ACS Applied Materials & Interfaces*, *15*(8), pp.10696-10708.
 18. Kavinkumar, T., Yang, H., Sivagurunathan, A.T., Jeong, H., Han, J.W. and Kim, D.H., 2023. Regulating Electronic Structure of Iron Nitride by Tungsten Nitride Nanosheets for Accelerated Overall Water Splitting. *Small*, p.2300963.
 19. Zhang, Z., Wang, Z., Zhang, H., Zhang, Z., Zhou, J., Hou, Y., Liu, P., Xu, B., Zhang, H. and Guo, J., 2023. Interface engineering of porous Co (OH)₂/La (OH)₃@ Cu nanowire heterostructures for high efficiency hydrogen evolution and overall water splitting. *Journal of Materials Chemistry A*, *11*(8), pp.4355-4364.
 20. Zhou, Y., Wu, Y., Guo, D., Li, J., Li, Y., Yang, X., Fu, S., Sui, G. and Chai, D.F., 2023. Novel Strain Engineering Combined with a Microscopic Pore Synergistic Modulated Strategy for Designing Lattice Tensile-Strained Porous V₂C-MXene for High-Performance Overall Water Splitting. *ACS applied materials & interfaces*, *15*(12), pp.15797-15809.
 21. Zang, Y., Lu, D.Q., Wang, K., Li, B., Peng, P., Lan, Y.Q. and Zang, S.Q., 2023. A pyrolysis-free Ni/Fe bimetallic electrocatalyst for overall water splitting. *Nature Communications*, *14*(1), p.1792.
 22. Wang, S., Zhang, Y., Deng, X., Ma, Z., Cheng, R., Wan, Z., Li, J. and Wang, X., 2023. Rational construction of loosely packed nickel nanoparticulates with residual HCOO ligands derived from a Ni-MOF for high-efficiency electrocatalytic overall water splitting. *Journal of Materials Chemistry A*, *11*(10), pp.5222-5232.
 23. Viswanathan, P. and Kim, K., 2023. In Situ Surface Restructuring of Amorphous Ni-Doped CoMo Phosphate-Based Three-Dimensional Networked Nanosheets: Highly Efficient and Durable Electrocatalyst for Overall Alkaline Water Splitting. *ACS Applied Materials & Interfaces*, *15*(13), pp.16571-16583.
 24. Li, G.L., Qiao, X.Y., Miao, Y.Y., Wang, T.Y. and Deng, F., 2023. Synergistic Effect of N-NiMoO₄/Ni Heterogeneous Interface with Oxygen Vacancies in N-NiMoO₄/Ni/CNTs for Superior Overall Water Splitting. *Small*, p.2207196.
 25. Sk, S., Madhu, R., Gavali, D.S., Bhasin, V., Thapa, R., Jha, S.N., Bhattacharyya, D., Kundu, S. and Pal, U., 2023. An ultrathin 2D NiCo-LDH nanosheet decorated NH₂-UiO-66 MOF-nanocomposite with exceptional chemical stability for electrocatalytic water splitting. *Journal of Materials Chemistry A*, *11*(19), pp.10309-10318.